Performance comparison of compact phased arrays and traditional seismic networks for microseismic monitoring at a CO_2 sequestration test site

Jian Zhang[1], Kevin D. Hutchenson[1], Paul A. Nyffenegger[1], Elige B. Grant[1], Jason Jennings[1], Mark A. Tinker[1], Marie Macquet[2], and Don C. Lawton[2,3]

https://doi.org/10.1190/tle42050332.1

Abstract

As carbon capture, utilization, and sequestration scales toward the gigatonnes level, the need for underground reservoir surveillance is driving efforts in advancing technologies for cost-effective passive seismic monitoring. Quantum Technology Sciences, in cooperation with Carbon Management Canada's Containment and Monitoring Institute (CaMI), installed a network of four permanent compact volumetric phased arrays (seismic and acoustic detection and ranging [SADAR] system) at CaMI's Field Research Station (FRS) to demonstrate the results that can be achieved through passive monitoring of microseismicity using this technology. Configured as a sparse network, the SADAR arrays provide passive, persistent, and permanent data acquisition and analysis for monitoring microseismicity in the earth volume of interest. Data from the phased arrays are processed to take advantage of the spatial coherence of the incident seismic signals to increase signal resolution while suppressing noise and clutter signals and providing signal attributes such as angle of incidence and phase velocity. The CaMI FRS has a network of 28 permanent surface stations that are deployed in an x-shaped geometry centered on the injection well. It has a downhole array of 24 geophones that are permanently deployed in an observation well. This provides a ready and unique opportunity to evaluate the detection and location performance of the different systems for passive seismic monitoring. We analyze observations of five example events selected from the microseismicity detected by the SADAR arrays with moment magnitudes (M_w) down to approximately –2. Signal-to-noise ratio (S/N) and location uncertainties are compared for the events acquired using SADAR arrays versus the surface sensors. The results demonstrate improved performance of networked SADAR arrays compared to traditional surface sensor deployment for detecting and locating microseismicity. Specifically, the results show that coherent processing of SADAR arrays achieves S/N gains up to about 20 dB and location errors down to 10 m.

Introduction

Passive monitoring for the sensing and characterization of induced seismicity associated with CO_2 injection is a persistent, economical, and effective measurement, monitoring, and verification technology. The technology contributes to managing risks associated with underground carbon sequestration, ensuring continued safety of ongoing operations and verifying ongoing reservoir integrity. At the gigatonne storage level, passive seismic systems are challenged with providing useful information in real time, as well as being cost effective, reliable, and maintainable for lifetimes extending well past the closure of injection. At the same time, the economic and logistical realities of required ongoing monitoring are steering managers toward permanently installed robust systems with the minimum number of channels, reduced infrastructure requirements, and minimal surface expression (e.g., Eaton, 2018).

Surface networks and/or downhole sensors are the most common microseismic monitoring deployments for detecting intentional and incidental induced seismicity associated with injection and production at geologic reservoirs. A large network of surface sensors permits acceptable accuracy in horizontal locations thanks to the wide network aperture. However, surface monitoring often suffers from low signal-to-noise ratio (S/N) due to high noise and/or large depth to the subsurface target. The low S/N contributes to microseismic monitoring results from surface sensor network data that have large uncertainties in constraining the location and depth of events. In addition, activities associated with the operation of any of these commercial installations result in a variety of sources in distributed locations. This creates a variety of noise signals that propagate to the sensors and clutter the acquired time series. Surface sensor networks attempt to mitigate this noise with sheer numbers, fielding very large and dense networks that enable frequency-wavenumber (*f-k*) and similar filtering techniques. These surface deployments may be expensive and, by design, require a large footprint. The effectiveness of *f-k* filtering will not generally be spatially uniform due to layout geometries relative to noise source locations. In addition, such deployments are usually temporary and do not constitute reliable permanent networks.

In contrast, siting downhole arrays close to the monitoring target and away from noise sources and energetic surface waves enables the detection of more events at lower magnitudes. However, reducing noise via deep borehole emplacements comes at an increased cost and complexity. It also sacrifices the surface sensor network advantages of deployment simplicity, flexibility, sampling density, and total spatial coverage for constraining the locations of events that may be distributed throughout a substantial earth volume.

An alternative is to deploy phased arrays of point sensors where the acquired data are processed coherently to maximize

[1]Quantum Technology Sciences, Melbourne, Florida, USA. E-mail: khutchenson@qtsi.com; pnyffenegger@qtsi.com; egrant@qtsi.com; jjennings@qtsi.com; mtinker@qtsi.com.
[2]Carbon Management Canada, Calgary, Alberta, Canada. E-mail: marie.macquet@cmcghg.com; don.lawton@cmcghg.com.
[3]University of Calgary, Calgary, Alberta, Canada.

the received signal at the array. In this paper, we use the term "phased array" in the traditional sense described in Van Trees (2002) and as defined for radar (e.g., Frank and Richards, 2008), sonar (e.g., Ziomek, 1995), and acoustics (e.g., Michel, 2006), with the constraint that the arrays here are used strictly as passive receivers. Phased arrays are more than simply the receiver groups commonly used in active-source seismic surveys, where the individual sensors provide data that are then summed into a single channel. For example, in the phased arrays discussed here, the point sensors are always acquired as individual channels. One or more design frequencies are used in planning the relative geometries of the array elements (also known as stations) to enable beam steering in arbitrary directions. Compared to receiver groups, basic phased array processing produces multiple beams simultaneously, with a greatly improved directivity index and with a beam response pattern that varies minimally as the beam main response axis (MRA) vector varies. Additionally, using properly designed phased arrays allows application of the extensive techniques discussed in the large volume of array signal processing literature. A complete comparison of phased arrays and receiver groups is beyond the scope of this work. The reader is referred to the previous citations on phased arrays, as well as Cordsen et al. (2000), Baeten et al. (2001), Cortes et al. (2015), and Criss (2019) as examples of documentation on receiver groups.

Quantum Technology Sciences has developed passive, permanent, and compact volumetric phased arrays using the principles of real-time data processing, specifically for seismic and acoustic detection and ranging (SADAR) systems for security, surveillance, and industrial applications. The primary goals of using compact volumetric phased arrays in these applications are to optimize the S/N of the received signal, determine the unambiguous angle of arrival, and determine the phase velocity of the arriving signal. Using the compact volumetric phased arrays, the SADAR system also offers an ability to mitigate coherent noise signals arriving from arbitrary directions and separate unrelated simultaneously arriving signals that cover the same frequency spectrum but originate with sources at different locations. Neither is possible with small-aperture arrays (e.g., Swanson and Culver, 2017). Moreover, using the SADAR system enables array S/N gains approaching the theoretical maximum of 10 log N decibels for N elements. This is generally not attainable for small-aperture arrays or receiver groups.

Similar phased arrays have previously been used for global and regional monitoring for nuclear treaty enforcement, focusing on very long period signals originating with large seismic events and their multipath and multimode arrivals. Primarily due to the large wavelengths of the received signals, these seismic monitoring arrays are deployed in a mostly horizontal plane as single arrays in a global network of sensors and arrays (see Douglas [2013] for a review).

Regardless of the arrangement of array elements, fielding a phased array enables spatial-coherence processing methods to be applied to the collected data to increase the coherent signal relative to the noise and extract additional information that can only be provided by a phased array. By taking advantage of the 3D array response and spatially coherent processing (beamforming), the SADAR system optimally suppresses noncoherent and coherent noise arriving from directions other than the beam MRA. It does this while increasing coherent S/N prior to event detection and reducing the uncertainty in determining phase arrival times, especially for low S/N events. Finally, the data processing workflow for reducing the acquired raw signals to event locations, characteristics, and patterns lends itself to automation for real-time reporting.

The Containment and Monitoring Institute (CaMI) constructed and operates a Field Research Station (FRS) as a CO_2 storage test site in southern Alberta, Canada (Figure 1a). At the FRS, small volumes of CO_2 (about 30 tons/year) are injected into the

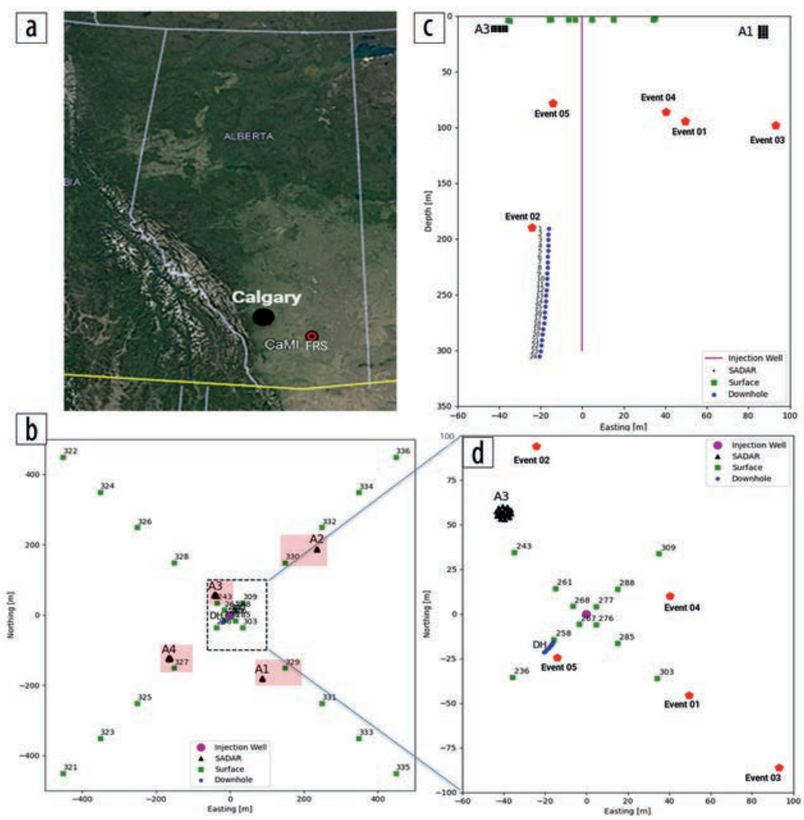

Figure 1. CaMI FRS seismic monitoring systems. (a) CaMI FRS site location. (b) Map view of CaMI FRS seismic monitoring networks centered at the injection well (magenta dot). The locations of the SADAR arrays (black triangles), surface network (green squares), and downhole array (blue dots). (c) Side view of the downhole array (blue dots), injection well (magenta line), surface sensors (green squares), SADAR array A3, and five study events (red stars). Note the different scale of the easting and depth. (d) Zoomed-in map view of the area in the dashed square in (b) with the epicenter locations of the five study events (red stars).

reservoir formed by the Basal Belly River Sandstone Formation at 300 m depth (Lawton et al., 2019). One of the purposes of the CaMI FRS is to support the research and development of monitoring technologies for detecting and locating seismicity that could be associated with potential CO_2 leakage (Macquet et al., 2022). Among the permanently deployed seismic instruments at the FRS (Macquet and Lawton, 2019), a surface network of 28 three-component geophones buried at 1 m depth (green squares in Figure 1), as well as a downhole array of 24 three-component geophones (blue dots in Figure 1), remain actively recording as a passive network. Quantum Technology Sciences, in collaboration with CaMI, deployed a sparse network of four SADAR arrays at the FRS in November 2021 (black triangles in Figure 1). Simultaneous monitoring at the FRS using multiple networks provides a unique opportunity to compare the detection and location performance. With the observations and analysis of five typical microseismic events, we demonstrate that a network of passive, persistent, permanent, and compact volumetric phased arrays delivers multiple technical advantages over traditional surface networks or downhole deployments for monitoring microseismic activity at production, injection, and CO_2 sequestration sites. In comparison with surface and near-surface dense seismic deployments, SADAR arrays offer a reduced surface footprint, enhanced signal detection, and enhanced signal characterization capabilities. This leads to a more complete understanding of the incident seismic signals.

Phased array design and deployment

Three SADAR array designs with between 51 and 72 elements and variations in geometry are being evaluated. All three phased array designs are configured as combinations of uniform cylindrical arrays (UCAs), with the topmost array sensor layer depth at 10 m. These designs enable the assessment of performance for reduced configurations (i.e., subsets) of array elements. The three array designs consist of:

a) The standard design consists of a 54-element octagonal UCA with a central column and six layers of elements as shown in Figure 2a and located at A1 and A2 in Figure 1.
b) The wide-aperture design consists of 51 elements in three layers and geometry of a hexagonal UCA with a central column within a larger horizontal-aperture decagonal UCA for a total of 17 boreholes as shown in Figures 2b and 2c and located at A3 in Figure 1.
c) The hybrid design consists of a 72-element array arranged as a hexagonal six-layer UCA with a central column within a larger horizontal-aperture decagonal six-layer UCA as shown in Figures 2b and 2d and located at A4 shown in Figure 1.

These SADAR arrays are designed with the sensors spaced along the perimeter of the UCAs at the ideal half-wavelength spacing for a horizontally incident wavefront at the design frequency. The layer spacing is similarly defined for a vertically incident wavefront. For example, for an element spacing of 2 m, the frequency that corresponds to the wavelength (4 m) at the specified phase velocity (800 m/s) across the array is defined as

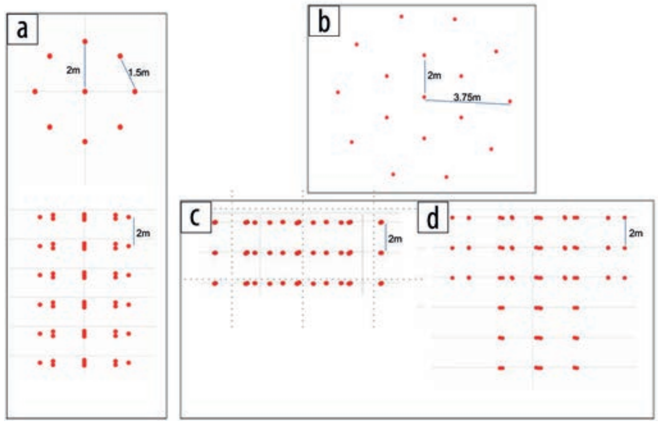

Figure 2. Layout of the installed and modeled arrays. (a) Standard octagonal UCA design with six layers. Map view is shown at the top, and depth cross section at the bottom. (b) Map view of the wide-aperture and hybrid array designs with 17 boreholes in a nested UCA pattern. (c) Depth cross section for the wide-aperture layout with three layers. (d) Depth cross section for the hybrid layout. The outer decagonal UCA has three layers, and the hexagonal inner UCA and central column has six layers.

the array design frequency (200 Hz). However, because seismic propagation involves multiple wave modes traveling at different phase velocities, an array with a single element spacing will correspond to more than one design frequency. Using multiple design frequencies has the benefits of broadening the array frequency response, shaping the overall primary beam in terms of directivity index, and suppressing and equalizing the response pattern side lobes. Furthermore, in the designs presented here, there is a wide diversity of interelement spacings that contribute to a desirable array response for frequencies below the design frequencies.

Candidate 3D array geometries were modeled for exploring the array response for selected wavefront incidence angles and signal frequencies. The model assumes omnidirectional point sensors for array elements and an incoming plane wave of a single wavelength (i.e., single frequency). Other than the array element geometry, the parameters required for the model include the propagation phase velocity across the array and the frequency, azimuth, and dip angle for the incident wavefront. The example beam patterns shown in Figure 3 demonstrate the response of each array design in terms of the directivity index in decibels relative to a theoretical isotropic sensor (i.e., an omnidirectional sensor). This is specific to the wavefront incidence geometry and the wavelength derived from user-supplied phase velocity and frequency for the ideal case where the incident wave frequency matches the array design frequency. The beam width, as indicated by the value of the directivity index, correlates with the resolution in azimuth and dip and is controlled by the array aperture in the plane of the wavefront. The ideal beam MRA is aligned normal to the incident wavefront, with the strongest side lobe mirrored about the x–y symmetry plane caused primarily by the symmetry in the array. The magnitude of the side lobes represents the ability of the array to reject coherent waves with arrival angles not aligned with the beam MRA (i.e., off-MRA rejection). The main beam generated from array design (a) was typically wide laterally, with better resolution in the z direction. In comparison, the (b) and (c) array geometries with a wider horizontal aperture produce main beams with greater resolution in the horizontal plane. However, the additional

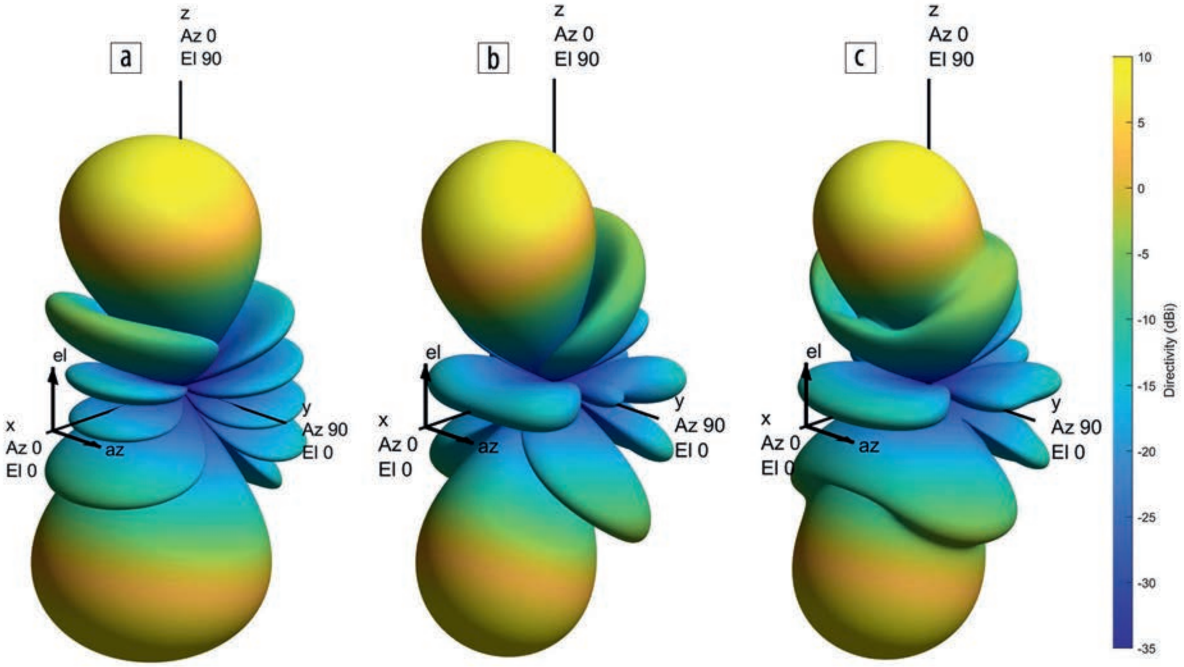

Figure 3. Modeled array response in terms of directivity index in decibels relative to a theoretical isotropic sensor for the (a) standard, (b) wide-aperture, and (c) hybrid SADAR array designs. The displayed responses are computed for a monochromatic incident wave with geometry azimuth = 0° and elevation = –70° (i.e., an upward propagating wave incident upon the array). In this ideal case, the frequency of the incident wave matches the array design frequency for the 2 m interlayer spacing. Two sets of axes are used in each plot. Cartesian coordinates are displayed because that system is used to specify the positions of the array elements. However, the response of the array is computed relative to the array reference point (in this case the centroid) and is naturally in a spherical coordinate system of azimuth and elevation (or dip). The ideal beam MRA is aligned from the array reference point through the maximum of the main lobe (pointing downward at 70°). The off-MRA rejection potential for coherent signals incident at other azimuth and dip angles is shown as the side lobes.

Table 1. Event parameters determined from SADAR network data: origin date and time, location in decimal degrees and in meters relative to the reference injection well location, depth in meters, and M_w.

	Date	UTC time	Latitude	Longitude	X (m)	Y (m)	Depth (m)	M_w
Event 01	2021 Nov 18	16:25:48.465	50.45002N	112.11997W	49.71	–45.62	94	–1.2
Event 02	2022 Jan 21	18:07:38.244	50.45127N	112.12104W	–24.27	93.93	189	–1.3
Event 03	2022 Jan 21	19:36:09.672	50.44967N	112.11935W	93.02	–85.91	98	–0.8
Event 04	2022 Feb 18	17:36:41.026	50.45052N	112.12011W	40.24	10.10	86	–1.5
Event 05	2021 Dec 07	15:23:06.285	50.45020N	112.12087W	–14.11	–24.44	78	–1.9

layers for array designs (a) and (c) increase the aperture in the z direction, resulting in suppressed side lobes compared with (b). Although not shown in Figure 3, increasing the number of elements (at the proper spacing) always increases the array gain; however, it does not always result in tighter beam widths or improved side lobe suppression. Lastly, applying common array processing methods allows additional gains of S/N for signals with angle of arrival within the beam main lobe while minimizing side lobes and mitigating effects of coherent noise sources.

Four arrays (two of design [a] and one each of designs [b] and [c]) were installed at distances that ranged between 70 and 300 m from the injection well (Figure 1) at depths about 10 m below ground surface to the uppermost sensors. For each array, individual borehole locations were surveyed using a combination of GPS and handheld measuring devices. A lightweight drill rig bored 4-in holes with an auger bit to the required depth. Then, each hole was grouted from bottom to top to ensure that the borehole was without voids. The sensor string was then pushed through the grout by hand with a tool. The bottom sensor was protected by a wire cage to avoid damage. The array elements consist of cabled strings of Geospace GS-ONE 10 Hz vertical geophones, with each sensor attached to a dedicated 24-bit digitizer set at 2000 samples/s. To ensure synchronized timing across all of the arrays/elements, all data acquisition and logging connections are cabled and coordinated through a single Geospace GeoRes system with a GPS time source.

Data for performance evaluation

Since deployment in November 2021, the SADAR network at the FRS has been continuously detecting and locating microseismicity down to moment magnitude (M_w) –3 near the injection well (Nyffenegger et al., 2022; Zhang et al., 2022). Barring ground-truth events at depth, the performance of the monitoring networks can be evaluated by quantifying the signal quality (S/N) and location uncertainty level of representative events. Five events (Table 1) with magnitudes ranging between –0.8 and –1.9 were selected from the reviewed microseismic event bulletin (a subset of the total detected events). The event locations determined from using the phase picks at the SADAR arrays are shown in Figure 1.

All five events are located above the downhole array.

Figure 4 shows the signals of the first selected event ($M_w = -1.2$) recorded by the downhole array. Clear P-wave energy can be observed across the 24 downhole sensors, and the moveout confirms that the event is above the downhole array. However, the one-sided array event geometry and the lack of shear-wave arrivals places great challenges on locating these events with the downhole array alone. Therefore, in the following analysis we focus on performance evaluation by comparing the SADAR and surface networks.

The record section of the first selected event recorded by the surface network (Figure 5) shows the signals organized by the ascending distance from the event location to each of the surface geophones. Modeled P-arrivals are plotted on each of the three components, confirming that P-waves appear strongest on the vertical component. For a typical strong event near the injection well, the P-arrivals can be picked only at the surface geophones deployed at close range to the injection well (i.e., sensor IDs from 263 to 309; Figure 1d).

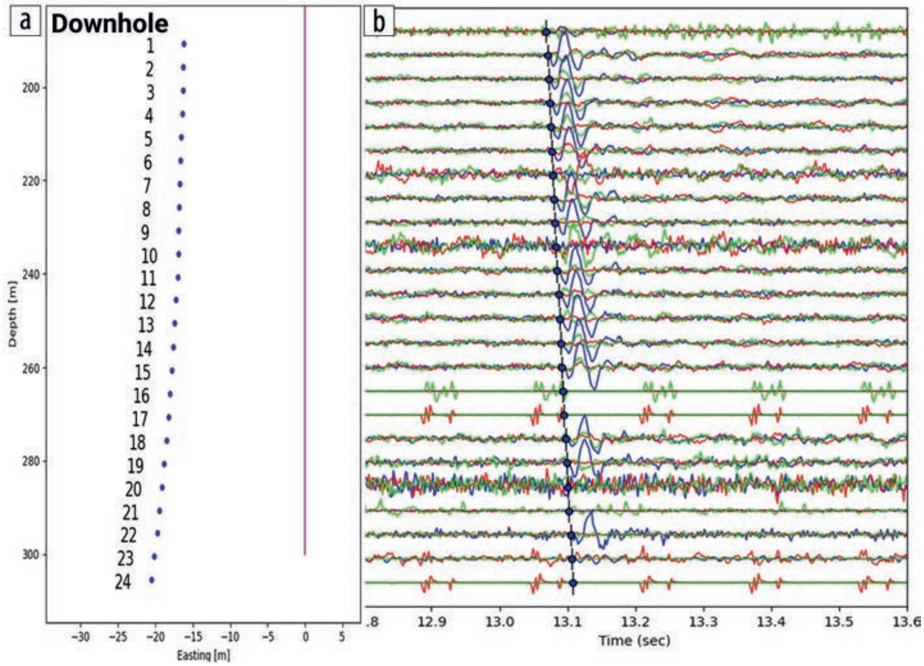

Figure 4. Downhole observations of event 01. (a) Record section is organized by matching the sensors from (b) top to bottom. Waveforms are shown for three components of vertical (blue), inline (red), and crossline (green). Black bars and dots mark the model-predicted arrival times based on the event location from using the SADAR network.

Data processing

The first step of the performance analysis is to determine the phase arrivals across the SADAR network and the surface geophones, respectively. For each of the four SADAR arrays, phase arrival picking is done on the optimal beam (i.e., the beam that optimizes the received signal power instead of individual array channels). The optimal beam is constructed for each array by the stack of signals at individual elements after using the azimuth, dip, and phase velocity information resulting from the *f-k* grid search across the 3D slowness domain. Evaluation of signal quality is straightforward by calculating S/N, which is defined as the maximum signal amplitude divided by the standard deviation of the series amplitudes in the data frame buffer ahead of the signal in physical units of velocity. Specifically, maximum signal amplitude is measured within a 0.3 s frame after the phase arrival pick. The noise is measured within a 0.2 s frame prior to the phase arrival pick time. The gain in the S/N is calculated as the ratio of the measured values from the SADAR array's optimal beam (S/N1) to the measured values from the surface sensors closest to each SADAR array (S/N2), cast into decibels using 20log(S/N1 / S/N2). As illustrated in Figures 1 and 6c, the SADAR arrays A1, A2, A3, and A4 are paired with the surface sensors with IDs 329, 330, 243, and 327 respectively.

Location performance is evaluated by using first-arrival phase picks and running the traditional single-event location method based on the work of Geiger (1910). Geiger's method essentially linearizes the relationship between arrival times and hypocentral parameters via a velocity model. Several iterations are performed until traveltime residuals reach a minimum defining the location solution. Note that additional attributes such as signal azimuth uniquely resulting from the phased array analysis (although providing optional constraints for inverting event locations) were not used in this study because we focused on demonstrating the performance difference using SADAR arrays exclusively due to S/N improvement. The initial event location estimate required for Geiger's method comes from a grid-search method similar to the source-scanning algorithm defined by Kao and Shan (2004). Location uncertainty is estimated by following Flinn (1965), Jordan and Sverdrup (1981), and Bratt and Bache (1988). This enables the use of a priori information about data uncertainties (pick errors) to compute confidence/coverage error ellipsoids.

To ensure an equivalent calculation of location uncertainties across the two different networks of the SADAR versus the surface array, a priori estimates of the picking errors δt (in seconds) are assigned to each individual phase time by using a common empirical linear relationship as a function of the S/N of the phase arrival:

$$\delta t \;=\; \max(round([-0.000123374 \times S/N + 0.008944306] \times 1000)/1000,\, 0.001). \qquad (1)$$

To characterize the size of the events, we follow Shearer (2009) and estimate M_w using the displacement spectrum corrected for the loss in amplitude due to propagation effects and fitted by the Brune (1970) model. Note also that the waveform data processed and shown are band-pass filtered between 30 and 90 Hz. Most of the microseismic events detected at this site have positive S/N within that band.

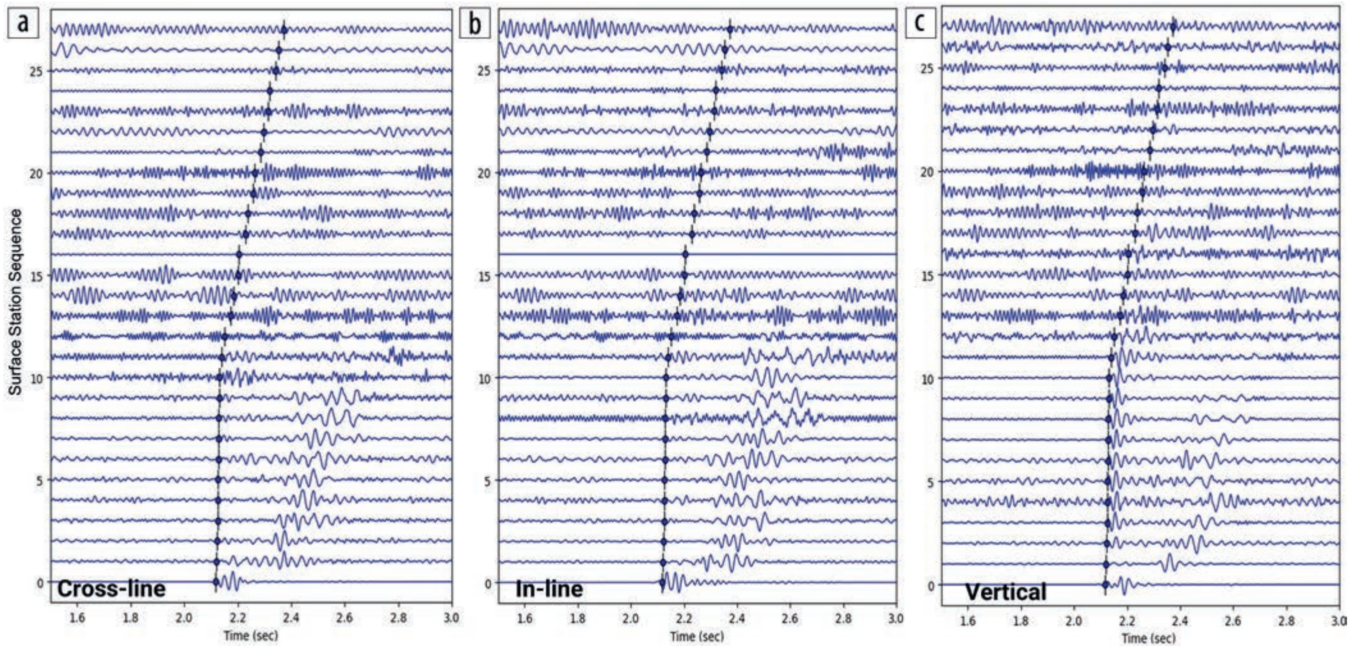

Figure 5. Surface observations of event 01: (a) crossline, (b) inline, and (c) vertical. Record sections are organized by ascending distance of the sensors to the event. Black bars and dots mark the model-predicted arrival times based on the event location from using the SADAR network.

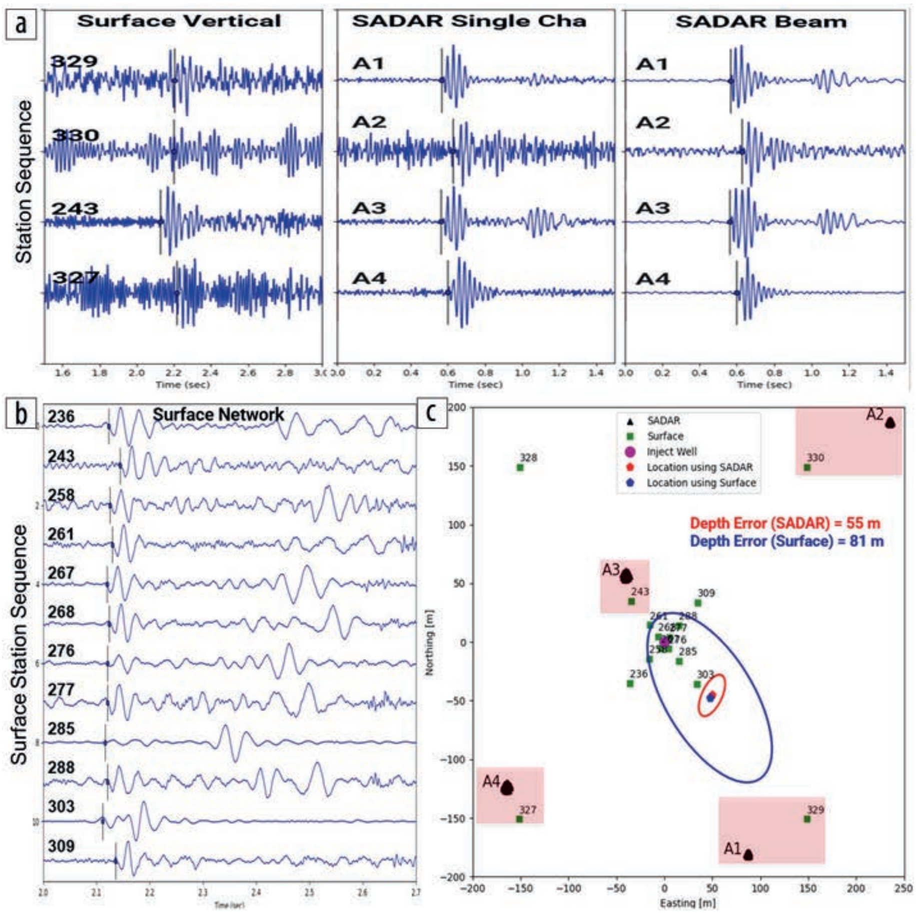

Figure 6. Comparison of the observations from the SADAR network versus the surface network for event 01. (a) Recorded event signals across the four surface sensors closest to each of the SADAR arrays compared with the four SADAR arrays top-layer center channel and optimal beam, respectively. (b) Signals on the vertical component across the close-range surface stations from ID 236 to 309. Black bars and dots mark the model-predicted arrival times. (c) Map view of the injection well (magenta dot), SADAR arrays (black triangles), surface network (green squares), event location estimate (stars), and error ellipses of the event locations from using the SADAR network (red) and surface network (blue). The red squares mark pairs of the SADAR arrays and the closest surface stations.

Array performance comparison

The first event (event 01 $M_w = -1.2$) represents a typical strong microseismic event with enough energy to be detected at multiple surface sensors. Figure 6a compares signals recorded at the surface stations 329, 330, 243, and 327 with signals at SADAR arrays A1, A2, A3, and A4. The first arrivals can be clearly picked at individual elements across all four SADAR arrays. The S/N is further improved by constructing optimal beams. In contrast, signals on the surface sensors closest to each SADAR array are much weaker and may not contribute to a clear detection and phase arrival estimation, even though the surface sensors have about the same event sensor range. Only surface station IDs 236–309 at a very close range to the event hypocenter record clear first arrivals (Figure 6b).

After picking the phase arrivals and obtaining the initial hypocenter estimate from source scanning, we perform single-event location using the four arrays of the SADAR network and surface network stations 236 to 309, respectively. Phase time errors are assigned using the measured S/N and the empirical relation defined by equation 1. The resulting locations and 95% coverage error ellipses are shown in Figure 6c. Despite using only four phase arrivals, the SADAR network can effectively constrain the event location within 20 m (error ellipse semimajor axis of 20 m and semiminor axis of 10 m) in epicenter and 55 m in depth. The location derived from the surface sensor network shows a greater uncertainty with the error ellipse semimajor axis of 87 m, semiminor axis of 43 m, and 81 m in depth due to the larger phase pick errors and the uneven sensor distribution, despite incorporating as many as 12 phase arrival picks.

Three other relatively large-size events with diverse distances to the injection well and depth are shown in Figure 7 (event 02 $M_w = -1.3$), Figure 8 (event 03 $M_w = -0.8$), and Figure 9 (event 04 $M_w = -1.5$). The observations are similar to the first event. In general, signals of events of this magnitude can show up at the surface stations with sensor-event ranges up to about 300 m. However, phase arrival times can only be confidently picked at close-range distances. This results in relatively large location uncertainties of up to a few hundred meters. On the other hand, S/N improvement at the SADAR arrays is evident from the comparison observations of all of these events. Furthermore, the common observation is that using only four time picks from the optimal beams derived from the SADAR arrays achieves a much

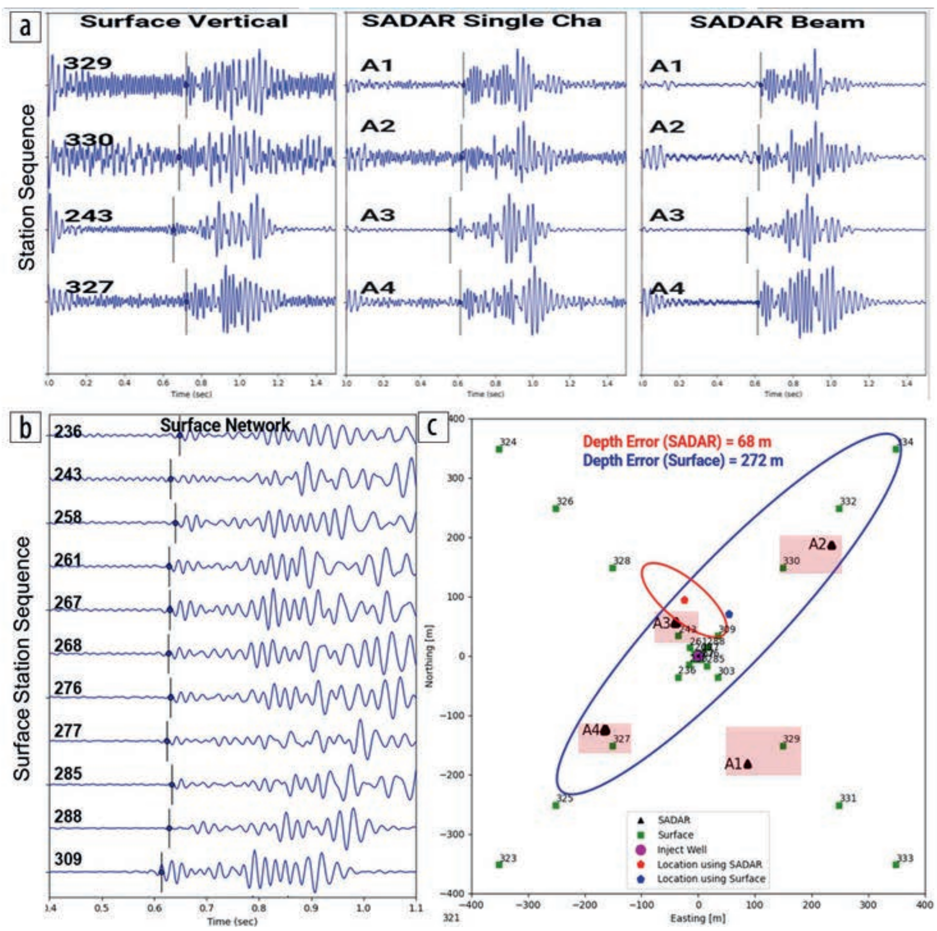

Figure 7. Comparison of the observations from the SADAR network versus the surface network for event 02. (a) Recorded event signals across the four surface sensors closest to each of the SADAR arrays compared with the four SADAR arrays top-layer center channel and optimal beam, respectively. (b) Signals on the vertical component across the close-range surface stations from ID 236 to 309. Black bars and dots mark the model-predicted arrival times. (c) Map view of the injection well (magenta dot), SADAR arrays (black triangles), surface network (green squares), event location estimate (stars), and error ellipses of the event locations from using the SADAR network (red) and surface network (blue). The red squares mark pairs of the SADAR arrays and the closest surface stations.

better location resolution and obtains an improved location performance compared to the surface network that typically includes more than 12 arrival time picks.

The fifth event (event 05 $M_w = -1.9$) represents the magnitude of the majority of microseismic events we observed at the site. Figure 10 shows that the surface network has difficulty recording clear first arrivals, not only at the stations close to the SADAR arrays (Figure 10a) but also across the dense sensor coverage (IDs 236 to 309) closer to the event (Figure 10b). Therefore, the location using the surface network is largely uncertain (e.g., with a semimajor ellipse axis up to 640 m) due to poor S/N and large phase arrival pick errors. In contrast, signals detected using the arrays' optimal beams (Figure 10a) allow precise picks and result in much smaller location uncertainties (Figure 10c), with a 95% coverage error ellipse semimajor axis of 39 m, semiminor axis of 20 m, and depth error of 64 m.

The S/N gain comparing the four SADAR arrays and the closest surface stations for the five events as summarized in Table 2 indicates up to a 22 dB S/N difference. Location errors down to 10 m in terms of ellipse semimajor axis, semiminor axis, and depth are given in Table 3. The observations from the five events demonstrate that deploying compact volumetric phased arrays, compared to traditional surface installations, greatly improves S/N. This enables microseismic event detection down to a smaller magnitude limit and thus a greater number of located events. The results in Table 3 also show that a straightforward benefit of higher S/N using compact phased arrays is that the errors in location estimates can be better quantified. It is worth noting that the focus in this study is on relative locations and the uncertainty in the determination of the event hypocenter. Analysis of absolute location performance relies on an accurate velocity model and calibration using ground-truth events and is beyond the scope of this work.

In addition, and as previously noted, the downhole array (Figure 4) offers little in the location of events within the area. While clear P-wave energy can be observed, moveout only confirms that the event locations are above the array. There are too many challenges to location with this array, due to the lack of additional borehole data and clear shear-wave phase arrivals.

Discussion and conclusion

A primary goal of passive seismic monitoring is to better understand geologic reservoir dynamics over the life of the field. As an

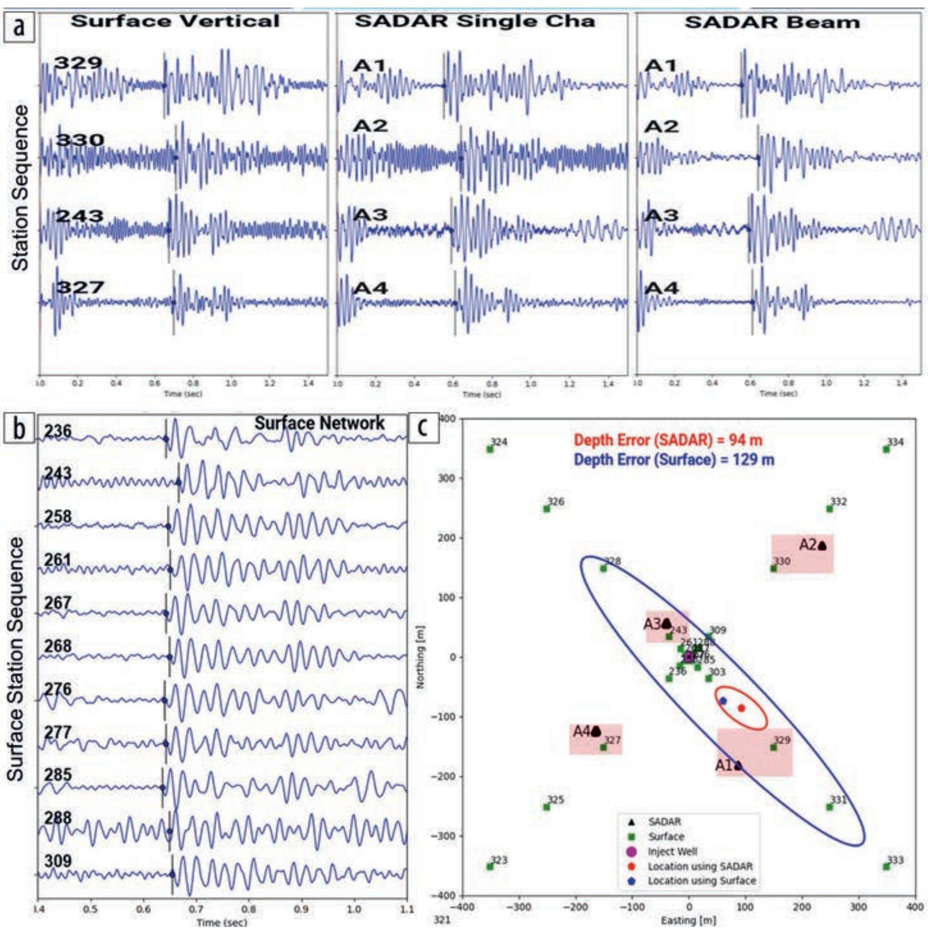

Figure 8. Comparison of the observations from the SADAR network versus the surface network for event 03. (a) Recorded event signals across the four surface sensors closest to each of the SADAR arrays compared with the four SADAR arrays top-layer center channel and optimal beam, respectively. (b) Signals on the vertical component across the close-range surface stations from ID 236 to 309. Black bars and dots mark the model-predicted arrival times. (c) Map view of the injection well (magenta dot), SADAR arrays (black triangles), surface network (green squares), event location estimate (stars), and error ellipses of the event locations from using the SADAR network (red) and the surface network (blue). The red squares mark pairs of the SADAR arrays and the closest surface stations.

alternative to traditional surface and downhole passive monitoring techniques, the SADAR test network of four compact volumetric phased arrays was installed to assess the performance of the technology for monitoring seismicity at the CaMI FRS CO_2 injection site. We have demonstrated that coherent processing (beamforming) of the data acquired using these compact volumetric phased arrays results in two-fold S/N improvements and robust detection and location of microseismic events. Furthermore, we have demonstrated that deploying sensors at depths, along with a phased array design and commensurate processing techniques, greatly improves the detection threshold and location precision. Performance differences between the SADAR network and the traditional surface network are documented in terms of S/N gain (up to about 20 dB) and location uncertainty (down to about 10 m from using SADAR compared with about 30 m from using the surface network).

The performance comparison results serve as a proof-of-concept example for planning a reservoir monitoring strategy. To meet probability-of-detection and location (including depth) confidence requirements for microseismic events and/or the needs of monitoring a reservoir with large areal extent, a network with a large aperture may be desired. However, as demonstrated earlier, passive monitoring using a traditional surface network of seismic instruments may be effective only at close event sensor ranges, thus requiring a large and dense sensor network, resulting in unsupportable costs.

Our results suggest that a sparse network of compact volumetric phased arrays achieves effective subsurface monitoring and represents an innovative approach to persistent, permanent, and passive sensing for geologic carbon sequestration. Deploying a sparse network of SADAR arrays offers a microseismic monitoring solution that reduces the surface footprint compared to networks of surface-emplaced sensors while providing significant S/N improvements. The improved S/N supports a lower detection threshold for improved seismicity bulletin magnitude of completeness and reduced location

Table 2. The S/N gain of SADAR arrays compared to the closest surface stations (in decibels).

Event number Comparison pair	Event 01 $M_w = -1.2$	Event 02 $M_w = -1.3$	Event 03 $M_w = -0.8$	Event 04 $M_w = -1.5$	Event 05 $M_w = -1.9$
A1 versus Surf_329	22	11	14	12	18
A2 versus Surf_330	14	2	16	13	8
A3 versus Surf_243	12	13	5	4	20
A4 versus Surf_327	21	9	13	12	20

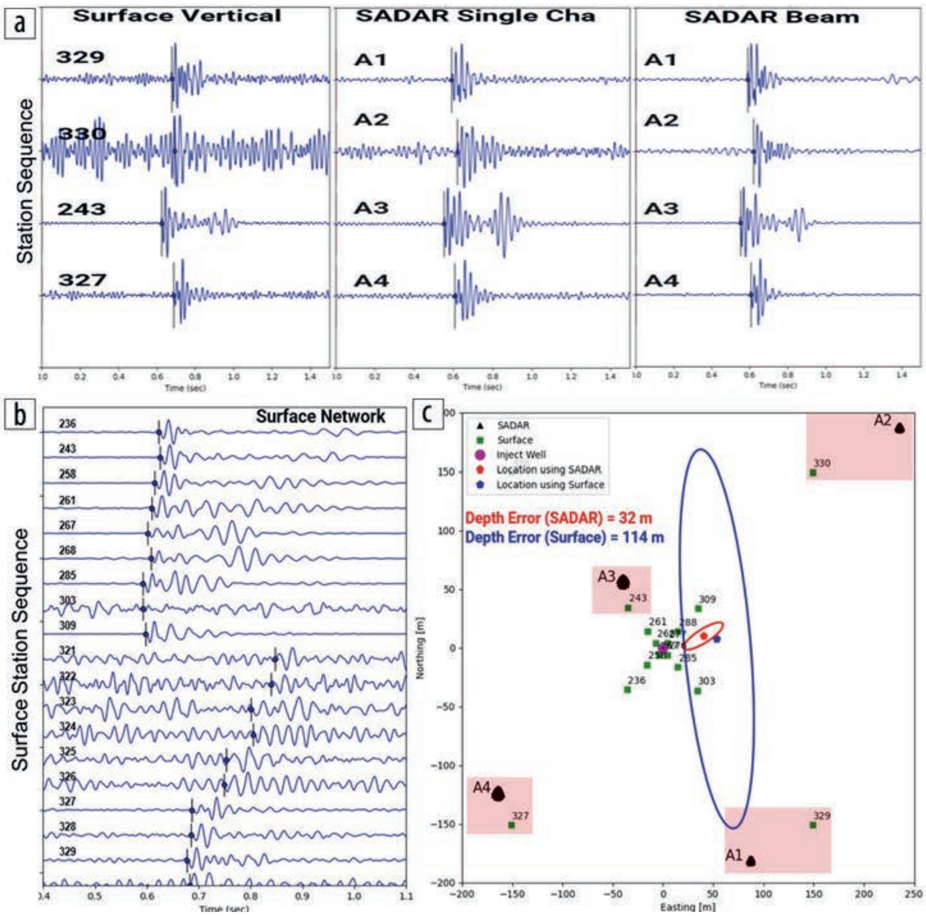

Figure 9. Comparison of the observations from the SADAR network versus the surface network for event 04. (a) Recorded event signals across the four surface sensors closest to each of the SADAR arrays compared with the four SADAR arrays top-layer center channel and optimal beam, respectively. (b) Signals on the vertical component across the close-range surface stations from ID 236 to 329. Black bars and dots mark the model-predicted arrival times. (c) Map view of the injection well (magenta dot), SADAR arrays (black triangles), surface network (green squares), event location estimate (stars), and error ellipses of the event locations from using the SADAR network (red) and the surface network (blue). The red squares mark pairs of the SADAR arrays and the closest surface stations.

uncertainty estimates. Additional attributes, such as unambiguous incident angles of the arriving energy and the true phase velocity across the array, are derivable only from coherent spatial processing of data acquired using volumetric phased arrays and not from traditional surface or downhole sensor deployments.

We expect that system performance will improve with array and network design improvements, including additional benefits from processing three-component geophones emplaced for array elements. With the addition of automated clutter-signal rejection algorithms, phase onset estimation algorithms, event clustering algorithms, and discrimination/classification stages, the demonstrated workflow will allow the automatic production of a real-time high-confidence seismic event bulletin and follow-on pattern analysis. Persistent monitoring technologies such as demonstrated here will be an enabling capability for measurement, monitoring, and verification of gigatonne-level CO_2 geologic sequestration reservoirs during active injection and post-closure phases. TLE

Table 3. Comparison of the location uncertainties in terms of horizontal 95% coverage error ellipse and depth estimated for locations from the SADAR network versus the surface network.

Event number Uncertainty		Event 01 $M_w = -1.2$	Event 02 $M_w = -1.3$	Event 03 $M_w = -0.8$	Event 04 $M_w = -1.5$	Event 05 $M_w = -1.9$
Ellipse semimajor axis (m)	SADAR	20	91	53	22	39
	Surface	87	420	343	162	640
Ellipse semiminor axis (m)	SADAR	10	35	23	6	20
	Surface	43	89	61	33	167
Depth (m)	SADAR	55	68	94	32	64
	Surface	81	272	129	114	1274

Acknowledgments

During the preparation of this manuscript, Jian Zhang, the primary author, tragically passed away. Jamie, as Jian was known to us, was a brilliant and dedicated scientist of multiple talents who was instrumental to this work, to our team, and to our company. He is sorely missed.

Quantum Technology Sciences Inc. is a wholly owned subsidiary of Geospace Technologies Corporation. We acknowledge Carbon Management Canada for providing access to the CaMI FRS to

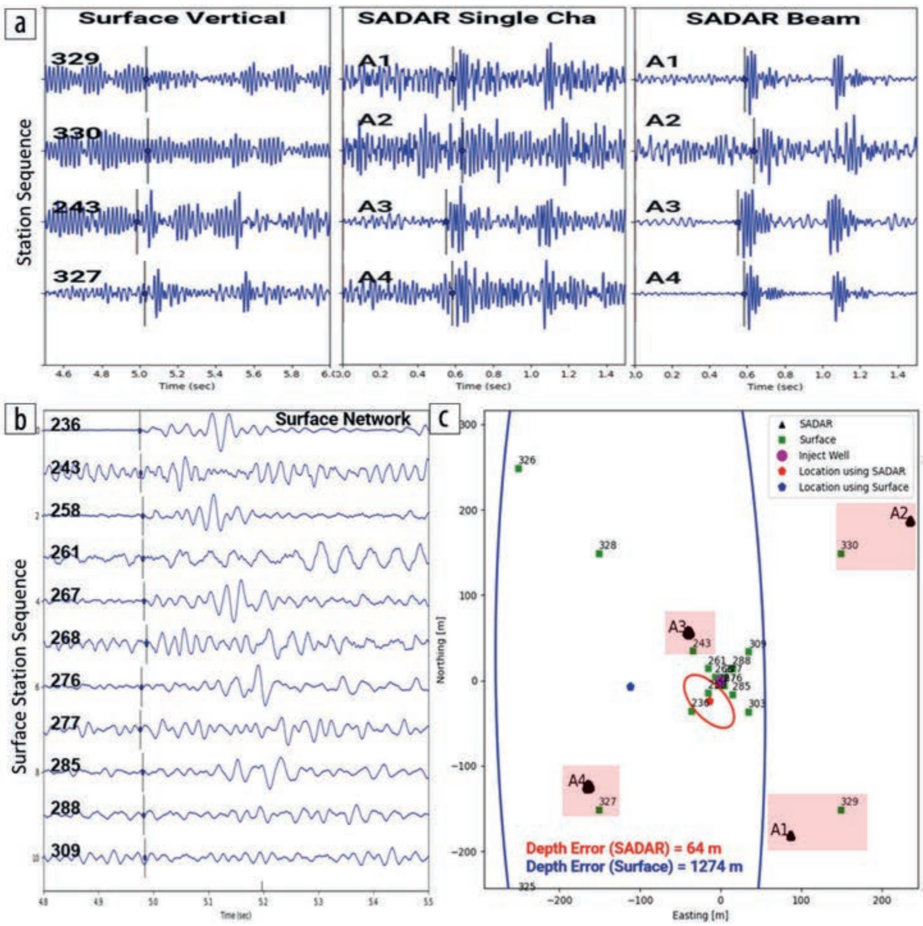

Figure 10. Comparison of the observations from the SADAR network versus the surface network for event 05. (a) Recorded event signals across the four surface sensors closest to each of the SADAR arrays compared with the four SADAR arrays top-layer center channel and optimal beam, respectively. (b) Signals on the vertical component across the close-range surface stations from ID 236 to 309. Black bars and dots mark the model-predicted arrival times. (c) Map view of the injection well (magenta dot), SADAR arrays (black triangles), surface network (green squares), event location estimate (stars), and error ellipses of the event locations from using the SADAR network (red) and the surface network (blue). Red squares mark pairs of the SADAR arrays and the closest surface stations.

enable installation of the SADAR system and for sharing the data from the surface and downhole networks. The FRS is supported by funding from the Global Research Initiative at the University of Calgary from the Canada First Research Excellence Fund and the CaMI Joint Industry Project. Carbon Management Canada is also acknowledged for providing operational data from the site.

Data and materials availability

Data associated with this research are confidential and cannot be released.

Corresponding author: pnyffenegger@qtsi.com

References

Baeten, G., V. Belougne, T. Brice, L. Commbee, E. Kragh, A. Laake, J. Martin, J. Orban, A. Özbek, and P. Vermeer, 2001, Acquisition and processing of single sensor seismic data: 15th Geophysical Conference, Australian Society of Exploration Geophysicists, Extended Abstracts, https://doi.org/10.1071/ASEG2001ab011.

Bratt, S. R., and T. C. Bache, 1988, Locating events with a sparse network of regional arrays: Bulletin of the Seismological Society of America, **78**, no. 2, 780–798, https://doi.org/10.1785/BSSA0780020780.

Brune, J. N., 1970, Tectonic stress and the spectra of seismic shear waves from earthquakes: Journal of Geophysical Research, **75**, no. 26, 4997–5009, https://doi.org/10.1029/JB075i026p04997.

Cordsen, A., M. Galbraith, and J. Peirce, 2000, Planning land 3-D seismic surveys: SEG, https://doi.org/10.1190/1.9781560801801.

Cortes, D. M., J. Caldwell, and C. González, 2015, Single geophone versus geophone array: A field study performed in Colombia: 85th Annual International Meeting, SEG, Expanded Abstracts, https://doi.org/10.1190/segam2015-5877389.1.

Criss, J., 2019, The enigma of arrays: First Break, **37**, no. 1, 45–47, https://doi.org/10.3997/1365-2397.n0006.

Douglas, A., 2013, Forensic seismology and nuclear test bans: Cambridge University Press, https://doi.org/10.1017/CBO9781139524001.

Eaton, D. W., 2018, Passive seismic monitoring of induced seismicity: Fundamental principles and application to energy technologies: Cambridge University Press, https://doi.org/10.1017/9781316535547.

Flinn, E. A., 1965, Signal analysis using rectilinearity and direction of particle motion: Proceedings of the IEEE, **53**, no. 12, 1874–1876, https://doi.org/10.1109/PROC.1965.4462.

Frank, J., and J. D. Richards, 2008, Phased array radar antennas, *in* M. I. Skolnik, ed., Radar handbook, third edition: McGraw-Hill, 13.1–13.74.

Geiger, L., 1910, Herdbestimmung bei erdbeben ans den ankunftzeiten: Nachrichten von der Gesellschaft der Wissenschaften zu Göttingen: Mathematisch-Physikalische Klasse, **4**, 331–349.

Jordan, T. H., and K. A. Sverdrup, 1981, Teleseismic location techniques and their application to earthquake clusters in the South-Central Pacific: Bulletin of the Seismological Society of America, **71**, no. 4, 1105–1130, https://doi.org/10.1785/BSSA0710041105.

Kao, H., and S.-J. Shan, 2004, The source-scanning algorithm: Mapping the distribution of seismic sources in time and space: Geophysical Journal International, **157**, no. 2, 589–594, https://doi.org/10.1111/j.1365-246X.2004.02276.x.

Lawton, D. C., J. Dongas, K. Osadetz, A. Saeedfar, and M. Macquet, 2019, Development and analysis of a geostatic model for shallow CO_2 injection at the Field Research Station, Southern Alberta, Canada, *in* T. Davis, M. Landrø, and M. Wilson, eds., Geophysics and geosequestration: Cambridge University Press, 280–296, https://doi.org/10.1017/9781316480724.017.

Macquet, M., D. Lawton, K. Osadetz, G. Maidment, M. Bertram, K. Hall, B. Kolkman-Quinn, et al., 2022, Overview of Carbon Management Canada's pilot-scale CO_2 injection site for developing and testing monitoring technologies for carbon capture and storage, and methane detection: Recorder, **47**, no. 1.

Macquet, M., and D. C. Lawton, 2019, Exploring continuous seismic data for monitoring CO_2 injection at the CaMI Field Research Station, Alberta, Canada: 89th Annual International Meeting, SEG, Expanded Abstracts, 4913–4917, https://doi.org/10.1190/segam2019-3216737.1.

Michel, U., 2006, History of acoustic beamforming: Presented at the Berlin Beamforming Conference.

Nyffenegger, P. A., M. A. Tinker, J. Zhang, E. B. Grant, K. D. Hutchenson, and D. C. Lawton, 2022, Compact phased arrays for microseismic monitoring: First Break, **40**, no. 4, 69–74, https://doi.org/10.3997/1365-2397.fb2022033.

Shearer, P., 2009, Introduction to seismology: Cambridge University Press.

Swanson, D. C., and R. L. Culver, 2017, Small-aperture array processing for passive multi-target angle of arrival estimation: The Journal of the Acoustical Society of America, **142**, no. 4, https://doi.org/10.1121/1.5006910.

Van Trees, H. L., 2002, Optimum array processing: Wiley, https://doi.org/10.1002/0471221104.

Zhang, J., E. B. Grant, P. A. Nyffenegger, M. A. Tinker, K. D. Hutchenson, and D. C. Lawton, 2022, Seismic monitoring using compact phased arrays: CO_2 sequestration monitoring: Second International Meeting for Applied Geoscience & Energy, SEG/AAPG, Expanded Abstracts, 483–487, https://doi.org/10.1190/image2022-3751162.1.

Ziomek, L. J., 1995, Fundamentals of acoustic field theory and space-time signal processing: CRC Press.